Projectile fragment emission in the fragmentation of ^{56}Fe on C, Al and CH_2 targets at 471 A MeV *

LI Yan-Jing(李彦晶)[1] ZHANG Dong-Hai(张东海)[2;1)] YAN Shi-Wei(晏世伟)[1,3] WANG Li-Chun(王立春)[1]
CHENG Jin-Xia(程锦霞)[1] LI Jun-Sheng(李俊生)[2] S. Kodaira[4] N. Yasuda[4]

[1] College of Nuclear Science and Technology, Beijing Normal University, Beijing 100875, China
[2] Institute of Modern Physics, Shanxi Normal University, Linfen 041004, China
[3] Beijing Radiation Center, Beijing 100875, China
[4] Fundamental Technology Center, National Institute of Radiological Sciences 4-9-1 Anagawa, Inage-ku, Chiba 263-8555, Japan

Abstract: The emission angle and the transverse momentum distributions of projectile fragments produced in the fragmentation of ^{56}Fe on CH_2, C and Al targets at 471 A MeV are measured. It is found that for the same target, the average value and width of the angular distribution decrease with an increase of the projectile fragment charge; for the same projectile fragment, the average value of the distribution increases and the width of the distribution decreases with increasing the target charge number. The transverse momentum distribution of a projectile fragment can be explained by a single Gaussian distribution and the averaged transverse momentum per nucleon decreases with the increase of the charge of projectile fragment. The cumulated squared transverse momentum distribution of a projectile fragment can be explained well by a single Rayleigh distribution. The temperature parameter of the emission source of the projectile fragment, calculated from the cumulated squared transverse momentum distribution, decreases with the increase of the size of the projectile fragment.

Key words: heavy ion, projectile fragmentation, transverse momentum distribution, CR-39

PACS: 25.70.-z, 25.70.Mn, 29.40.Wk **DOI:** 10.1088/1674-1137/38/1/014001

1 Introduction

The knowledge of heavy ion fragmentation at intermediate and high energy is very important in nuclear physics, astrophysics and medical physics. Considering the biological effects of space radiation, when astronauts have a mission outside Earth's magnetic field, they suffer from Galactic Cosmic Radiation(GCR) and solar particle events, e.g., showers of energetic charged particles from the surface of the Sun. These energetic charged particles are the dominant sources of the radiation dose and affect the health of people on long-duration spaceflight, both inside and outside the station. According to the GCR model developed by Badhwar and O'Neill [1], in unshielded free space in the inner heliosphere, iron ions deliver about 8% of the total dose from the GCR and 27% of the dose equivalent at times near the solar maximum, even though they contribute less than 1% of the total GCR flux. Because iron ions are the most densely ionizing particles which are present in significant numbers in the GCR, there has been considerable interest in understanding their transport through matter and their biological effects.

Understanding the radiobiology of heavy charged particles (HZE) is a subject of great interest due to the complicated dependence of their relative biological effectiveness on the type of ion and its energy, and its interaction with various targets. It has become clear that heavy ions have the largest radiological effects. These effects also appear in regions close to the beam entrance, i.e., in the depth-dose plateau region, where normal tissue is usually situated. In addition, due to the longer ranges of the fragments produced by the fragmentation of the incident ions, the tail of the dose distribution beyond the Bragg peak may be too high for minimizing the dose to normal tissue beyond the primary ion range. Finally, recent experimental results [2] have revealed that the projectile fragments are emitted at larger angles than the scattering angle of the beam, which further increases the spread of the beam. Exact information about the projectile fragment emission angular distribution will be especially important in radiotherapy. So far, only a few

Received 28 January 2013

∗ Supported by National Science Foundation of China (11075100, 10975019), Shanxi Provincial Foundation for Returned Overseas Chinese Scholars, China (2011-058) and Scientific Research Foundation for the Returned Overseas Chinese Scholars, Ministry of Personnel (MOP2006138)

1) E-mail: zhangdh@dns.sxnu.edu.cn

measurements have been performed to analyze projectile fragment emission angles from HZE reactions below 500 A MeV [2–4].

Fragmentation is a term commonly used to specify a nuclear disassembly by force. Hot fragmentation is meant to indicate the most violent of these processes, following excitation beyond the limits of nuclear binding, but still ending with bound nuclear fragments of different sizes in the final channel [5]. The formation mechanism of these fragments, whether they are the remnants of an incomplete destruction or the products of a condensation out of the disordered matter, has continued to be the topic of very active research. In order to describe the physical process of heavy ion transport, several one-dimensional Monte Carlo codes, such as HZETRN [6], HIBRAC [7], FLUKA [8], NUCFRAG2 [9] and three dimensional model [10] have appeared. The improved quantum molecular dynamics model (ImQMD) is a dynamical model which is developed to follow the reaction process on the microscopic level [11, 12].

The properties of ^{56}Fe on various targets at various energies have been studied by many groups [13–25], most of the studies are devoted to the total charge-changing cross sections and the partial cross sections of the projectile fragment productions, little attention is paid to studying the projectile fragment emission angular distribution.

In this paper, we present the results of the emission angular distribution, transverse momentum distribution and the temperature of emission source of a fragment produced in the fragmentation of 471 A MeV ^{56}Fe on C, Al and CH_2 targets. The CH_2 target is used to obtain the cross section on a hydrogen target. The fragmentation cross section was published in our previous paper [26]. The arrangements of this paper are as follows: we introduce our experimental details in Section 2. In Section 3, the experiment result and discussion are given. Lastly, we give the conclusion in Section 4.

2 Experimental details

2.1 Experiment

Stacks of C, Al and CH_2 targets sandwiched with CR-39 detectors were exposed normally to 471 A MeV ^{56}Fe beams at the Heavy Ion Medical Accelerator in Chiba (HIMAC) at the Japanese National Institute of Radiological Sciences (NIRS). Fig. 1 shows the configuration of a sandwiched target. A CR-39 sheet, about 0.77 mm in thickness, is placed before and after the targets. The thickness of the carbon, aluminum and polyethylene targets is 5, 3 and 10 mm, respectively.

After exposure, the CR-39 detectors were etched in 7N NaOH aqueous solution at a temperature of 70 ℃ for 15 hours. Then, the beam ions and their fragments manifest in the CR-39 as etch-pit cones on both sides of the CR-39 sheets. The images of ion tracks were scanned and analyzed automatically by the HSP-1000 microscope system and the PitFit track measurement software, then checked manually. The PitFit software allows us to extract some geometric information, such as the position coordinates, major and minor axes and areas of etched track spots on CR-39 surfaces. Image data (45 mm×45 mm) were acquired for both front and back surfaces of each CR-39 detector. About 2×10^4 Fe ions were traced from the first CR-39 detector surface in the stack. ^{56}Fe trajectories and the ones of secondary fragments were reconstructed in the whole stack.

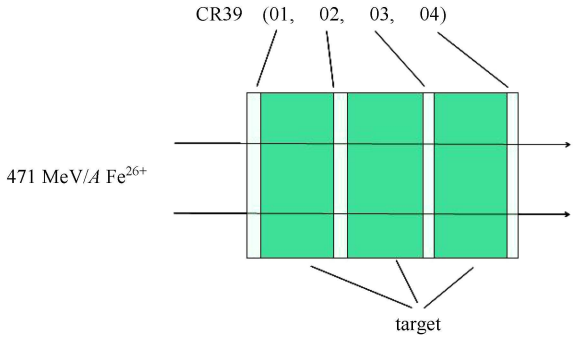

Fig. 1. (color online) Sketch of the target-detector configuration.

2.2 Ion track reconstruction

First, the spots on the front surface (with respect to the beam direction) are directly scanned, then the CR-39 sheet is turned under the middle line of the sheet and the spots on the back surface are scanned. The trajectories of ion tracks through CR-39 sheets are reconstructed in two steps using the track tracing method [27]: (1) the track position in CR-39 surfaces is corrected by a parallel and rotational coordinate translation (except for the track position on the upper surface of the first CR-39 sheet) and (2) the differences between the track positions of corresponding tracks on both sides of the CR-39 sheets and on the surfaces of the neighboring targets are minimized by a track matching routine. The track coordinate before the target (or the front surface of the CR-39 sheet) is (x, y) and of the matching track after the target (or the back surface of the CR-39 sheet) it is (x', y'). Following the translation relation, the coordinate of the matching track can be calculated as:

$$x'_{\rm th} = ax+by+c, \quad (1)$$

$$y'_{\rm th} = a'x+b'y+c', \quad (2)$$

parameters a, b, c, a', b' and c' are determined using the least square method. Then, the coordinate $x'_{\rm th}$, $y'_{\rm th}$ of the matching track are calculated. However, because of the Coulomb scatter etc. contributions, $x'_{\rm th}$, $y'_{\rm th}$ are certainly different from x',y', the difference $\mathrm{d}x=x'_{\rm th}-x'$, $\mathrm{d}y=y'_{\rm th}-y'$

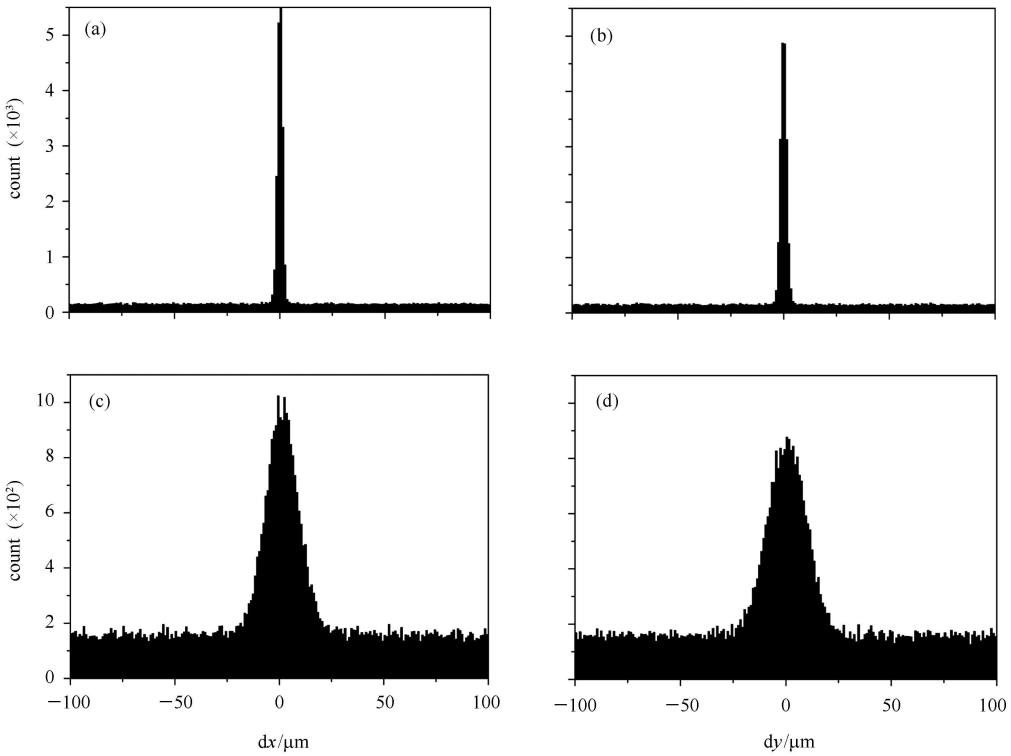

Fig. 2. The distribution of dx and dy. (a) and (b) the differences between the front and back surface on a CR-39 sheet, (c) and (d) the differences before and after carbon target.

are calculated, which can help us to determine the matching track.

Figures 2(a) and (b) show the differences, dx and dy, in the front surface and back surface on a CR-39 sheet, (c) and (d) show the differences, dx and dy, before and after the target. If the differences are calculated for all combinations of positions for extracted tracks, only the matching combinations ought to make a peak, which appears in Fig. 2, and the difference dx and dy of other combinations should be randomly distributed. The deviations $\sigma(x')$ and $\sigma(y')$ give the position accuracies of tracks, which are estimated to be 2–4 μm for the case of (a) and (b) and 8–20 μm for case of (c) and (d).

The matching iron ion tracks are searched within the $4\times\sigma(x')$ and $4\times\sigma(y')$ region of $x'_{\rm th}$ and $y'_{\rm th}$. The matching projectile fragments are searched within the limited fragmentation angle, which is about 10° in our experiment. The number of projectile fragments leaving the target are determined from the distribution of the etched area. Fig. 3 shows the track base area distribution of ^{56}Fe ions and their fragments in the CR-39 sheet. Peaks for ^{56}Fe and its fragments with the charge down to $Z=6$ appear clearly. Because of the limitation of the CR-39 detector, the tracks of fragments with charge $1 \leqslant Z \leqslant 5$ are not fully etched as measurable spots. The emission angle θ of each fragment is calculated by taking readings of the coordinates of the beam track and the fragment track.

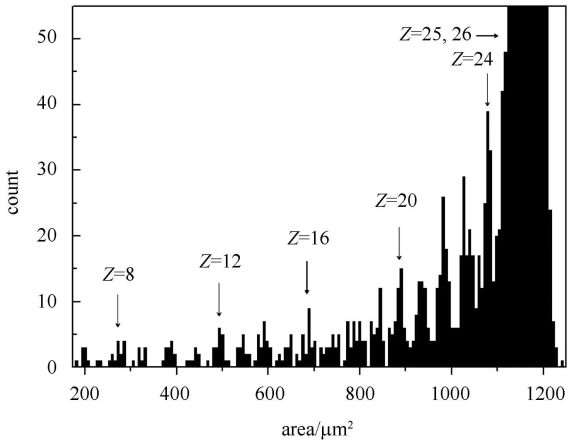

Fig. 3. The area distribution of etch-pit spots of all of the ^{56}Fe ions and the ones of secondary fragments on the CR-39 surface after CH_2 target.

3 Results and discussion

The emission angular distribution and transverse momentum distribution of projectile fragments provide information on the nuclear structure and the mechanism of nuclear interaction through which fragments are produced. These distributions are also very important in designing experiments with radioactive nuclear beams.

3.1 Angular distribution

The emission angle of each projectile fragment and the scattering angle of the iron ion are calculated from the coordinates of the track positions on the surface of the CR-39 sheet after the target. The angular uncertainty is determined using the quadruplet fitting method [4]

$$\sigma(\theta)=\frac{\sqrt{\sigma_z^2\sin^2\theta+2\sigma_{\rm p}^2\cos^2\theta}}{2h}, \quad (3)$$

where $\sigma_{\rm p}$ is the positional uncertainty in the x-y plane of the stack coordinate system, which is about 3 μm for the C-target, σ_z is the positional uncertainty in the z-axis that comes from the stack composition and detector thickness measurement and is estimated at ≈ 8 μm, θ represents the emission angle of the fitted line. With a detector thickness of $h\approx 780$ μm we thus obtain an angular uncertainty $\sigma(\theta)\approx 0.16^\circ$ for the value of θ up to 8°.

Figure 4 shows the angular distribution of primary iron ions and their fragments for different targets. The emission angle of primary iron ions mainly comes from the Coulomb scattering, most of which are less than 0.6°. Most of the projectile fragments have an emission angle less of than 1.5°, but some of the fragments have an emission angle up to 8°. The position of the maximum of the fragment angular distribution increases slightly with increase of the target mass, which can be explained as follows: with the increase of the target mass, the interaction between projectile and target is increased and so the influence the fragment suffered from the target is increased.

Figure 5 shows the emission angle distributions of projectile fragments with $Z = 6$, 18 and 24 produced from the fragmentation of ^{56}Fe on C and CH_2 targets; Fig. 6 shows the emission angle distributions of projectile fragments with $Z = 24$ and 25 produced from the fragmentation of ^{56}Fe on C, Al and CH_2 targets respectively. For fragments from the fragmentation of ^{56}Fe on C and Al targets, each angular distribution is fitted by a single Gaussian distribution, and for fragments from the fragmentation of ^{56}Fe on CH_2 target, each angular distribution is fitted by two Gaussian distributions; the fitting parameters including χ^2/DOF are presented in Table 1, where DOF means the degree of freedom of the simulation. From Figs. 5 and 6 and the results in Table 1, they show that for the same target, the average value and the width of the distribution decrease with increasing charge number of the projectile fragment; for the same projectile fragment, the average value of the distribution increases and the width of the distribution decreases with increasing the target charge number.

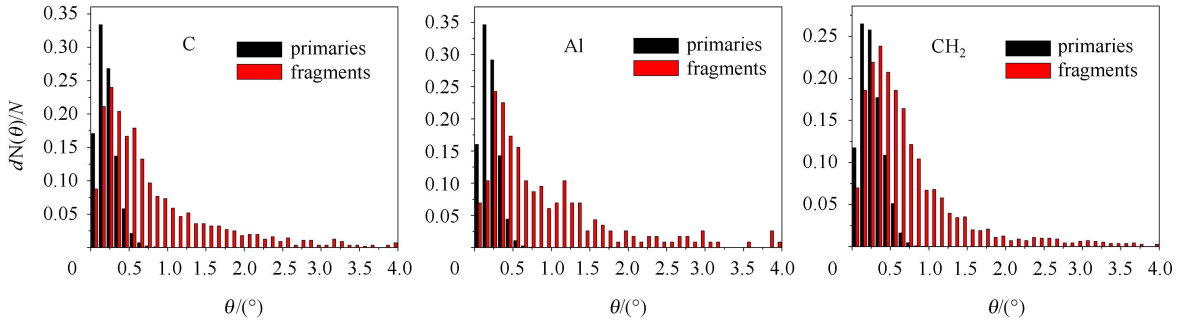

Fig. 4. (color online) The angular distribution of primary iron ions and their fragments for different targets; for comparison, the counts of fragments are enlarged two times.

Table 1. Values of fitting parameters of angular distribution using Gaussian distribution.

Z	target	percentage(1)	average value(1)	error(1)	percentage(2)	average value(2)	error(2)	χ^2/DOF
25	CH_2	16.382±5.523	0.251±0.021	0.127±0.026	7.325±2.923	0.488±0.172	0.279±0.077	1.123
	C	20.891±1.623	0.230±0.020	0.212±0.018				1.811
	Al	33.282±13.268	0.292±0.020	0.104±0.037				1.518
24	CH_2	17.734±1.495	0.385±0.017	0.213±0.017	1.435±0.538	1.133±0.107	0.183±0.160	1.153
	C	14.659±1.843	0.355±0.033	0.256±0.027				2.151
	Al	21.678±5.690	0.357±0.053	0.217±0.051				0.3067
18	CH_2	22.901±3.611	0.533±0.058	0.245±0.042	10.927±4.260	1.163±0.075	0.176±0.083	2.171
	C	16.000±3.579	0.620±0.121	0.537±0.142				0.4012
6	CH_2	13.708±0.952	1.864±0.337	1.725±0.308	0.300±1.064	2.969±1.072	0.040±1.439	0.1182
	C	10.744±3.658	2.035±0.335	1.778±0.809				1.008

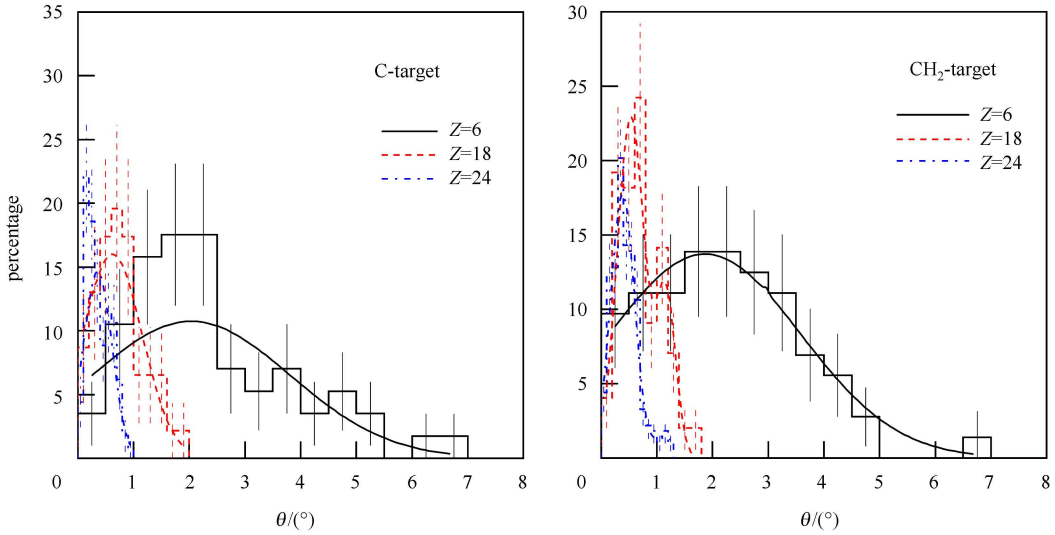

Fig. 5. (color online) The emission angle distributions of fragments with Z=6, 18 and 24, respectively.

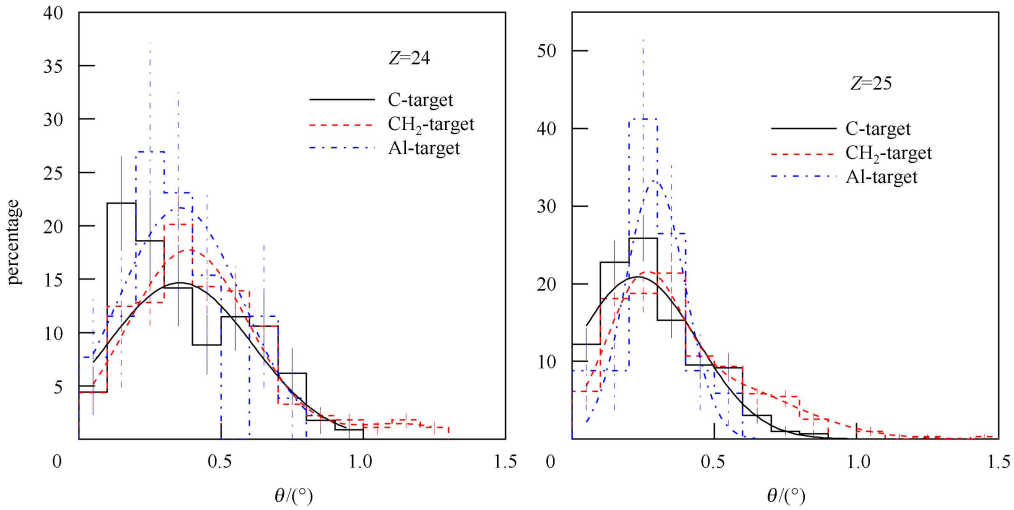

Fig. 6. (color online) The emission angle distributions of fragments with Z=24 and 25, respectively.

3.2 Transverse momentum distribution

The transverse momentum per nucleon (p_t) of a projectile fragment was calculated on the basis of its emission angle θ,

$$p_t = p\sin\theta, \tag{4}$$

where p is the momentum per nucleon of the beam, which can be calculated from the beam energy per nucleon (E), $p=(E^2+2m_0E)^{1/2}$. m_0 is the nucleon rest mass and θ is the emission angle of the projectile fragment with respect to the beam direction.

Figure 7 shows the transverse momentum distributions of a projectile fragment with Z=6, 18 and 24 produced from the fragmentation of ^{56}Fe on C and CH_2 targets. The distribution can be well fitted by a single Gaussian distribution, which is the same as the distributions of fragments produced in reactions of light projectiles [28, 29] and heavy projectiles [30–34] at relativistic energies. These Gaussians are in good agreement with predictions of the statistical model of Goldhaber [35]. This model assumes that the Fermi momenta of the nucleons in a fragment are statistically distributed as those in the original projectile nucleus. The averaged transverse momentum per nucleon for a fragment with Z=6, 18 and 24 are 35.89±35.25, 11.34±8.74 and 6.91±4.74 A MeV/c, respectively for the C target, and 34.38±30.79, 11.98±7.73 and 7.08±4.25 A MeV/c, respectively for the CH_2 target. For the same target, the averaged transverse momentum per nucleon and the width of the distribution increase with the decrease of the charge of the fragment. This tendency is also observed in Ref. [34].

Projectile fragments come from the directly produced

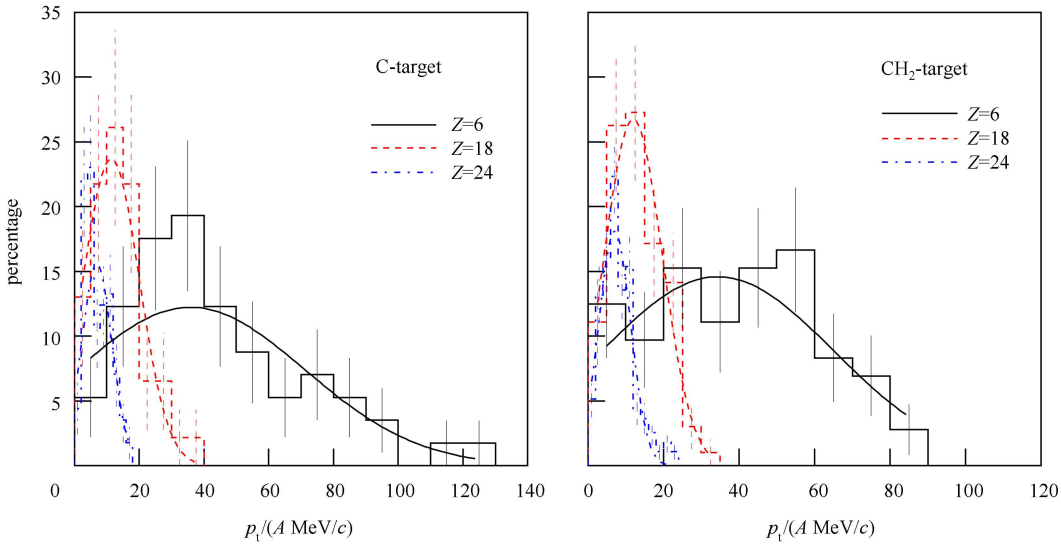

Fig. 7. (color online) The transverse momentum distributions of fragments with Z=6, 18 and 24, respectively.

fragments (primary fragments) and the sequential decay fragments from excited primary fragments. However, since the primary fragments are excited, they are de-excited by light particle evaporation. This secondary decay decreases the observed masses and increases the observed momentum widths of the primary fragments [36]. The contribution from sequential decay of primary fragments to the heavy projectile fragments is less than that to the light projectile fragments; the widths of the transverse momentum distributions of light projectile fragments are greater than those of the heavy projectile fragments. So the transverse momentum distribution width deceases with the increase of the charge of the projectile fragment, which is shown in Fig. 7.

Figure 8 shows the relation of the averaged transverse momentum per nucleon and the charge of projectile fragment for interactions of ^{56}Fe and C, Al and CH_2 targets. The averaged transverse momentum per nucleon decreases with the increase of fragment size; no obvious target size dependence is observed in this investigation. Fig. 9 shows the transverse momentum distribution of all projectile fragments for interactions of ^{56}Fe and C, Al and CH_2 targets; no obvious target size dependence is also observed. The heavy projectile fragment comes from a peripheral collision, which is a collision with a larger impact parameter. The light projectile fragment comes from a central and semi-central collision, which is a collision with a smaller impact parameter. According to the participant-spectator model [37], with the increase of the impact parameter, the overlapped region decreases and the communication between participant and spectator decreases. This results in a decrease of the excitation energy of projectile fragments, so the average transverse momentum of the projectile fragment is decreased.

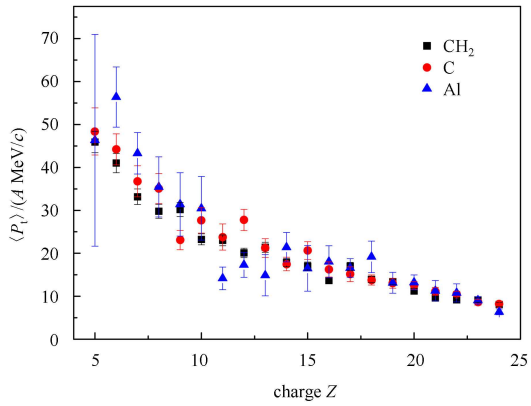

Fig. 8. (color online) Relation of the averaged transverse momentum and the charge of projectile fragment for interactions of ^{56}Fe and C, Al and CH_2 targets.

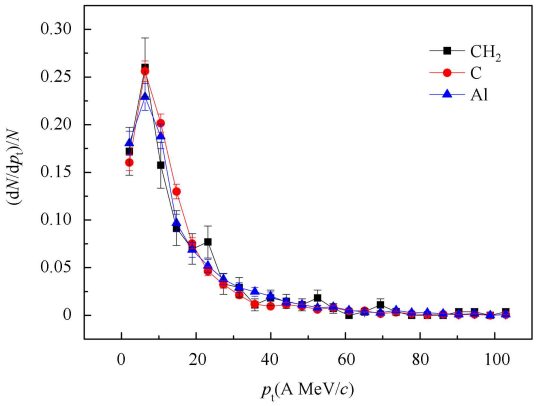

Fig. 9. (color online) Transverse momentum distribution of all fragments for interactions of ^{56}Fe and C, Al and CH_2 targets.

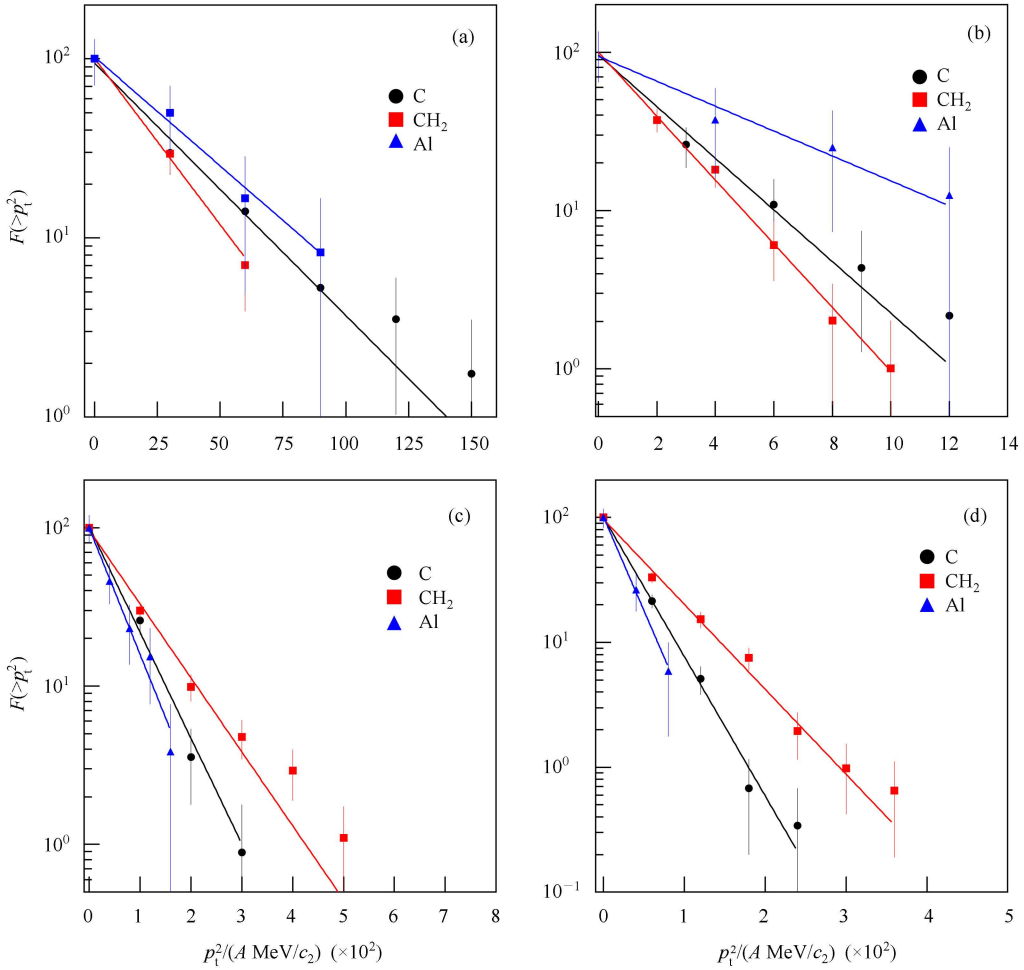

Fig. 10. (color online) The cumulative p_t^2 distribution of projectile fragments with $Z=6$ (a), $Z=18$ (b), $Z=24$ (c) and $Z=25$ (d).

Based on the participant-spectator concept and the fireball model [38], the large number of swept out nucleons combined with an anticipated fairly large number of interactions per particle is presumably responsible for the quasi-equilibrated system, i.e., the fireball which can then be described in terms of its mean value and statistical (Maxwell-Boltzmann) distribution. If we assume that the emission of projectile fragments is a Maxwell-Boltmann distribution in the projectile rest frame with a certain temperature T, then the integral frequency distribution of the square of the transverse momentum per nucleon is

$$\ln F(>p_t^2)=-\frac{A}{2M_pT}p_t^2, \tag{5}$$

where A is the mass number of the fragment and M_p is the mass of the proton. The linearity of such a plot would be strong evidence for a single temperature of the emission source.

Figure 10 shows the cumulative plots of $F(>p_t^2)$ as a function of p_t^2 for projectile fragments from the fragmentation of ^{56}Fe on C, Al and CH_2 targets. All of the plots can be well fitted by a single Rayleigh distribution of the form

$$F(p_t^2)=C\exp\left(\frac{-p_t^2}{2\sigma^2}\right), \tag{6}$$

where $\sigma=\sqrt{2/\pi}\langle p_t\rangle$, which is related to the temperature of the projectile fragment emission source, $T=\sigma^2A/M_p$. The fitting parameters including χ^2/DOF and the temperature of the emission source are presented in Table 2. Because the CR-39 detector cannot identify the mass numbers of projectile fragments, we use the mass number of a stable nucleus to calculate the temperature of the projectile fragment emission source. The influence from the isotope is less than 1% when an abundance of isotopes is considered. The dependence of the temperature of the emission source on the size of the projectile fragment for different targets is shown in Fig. 11. From the results of Table 2 and Fig. 11, we can conclude that the temperature of projectile fragment emission source decreases with the increase of the charge of projectile

Table 2. Values of fitting parameters of p_t^2 distribution using a Rayleigh distribution and the temperature of the emission source.

Z	target	C	$\sigma^2/((\mathrm{MeV}/c)^2)$	T/MeV	χ^2/DOF
25	CH_2	96.52±5.35	31.93±1.69	1.87±0.10	0.831
	C	100.16±5.71	19.47±1.11	1.14±0.07	0.235
	Al	100.56±16.91	14.50±2.78	0.85±0.16	0.033
24	CH_2	96.77±5.95	46.51±3.01	2.58±0.17	1.398
	C	101.72±9.24	32.52±2.89	1.80±0.16	0.575
	Al	99.56±17.90	27.25±5.00	1.51±0.28	0.159
18	CH_2	99.45±9.32	108.00±9.34	4.61±0.40	0.142
	C	95.86±14.60	133.30±22.31	5.68±0.95	0.310
	Al	94.08±33.96	276.24±127.42	11.78±5.43	0.108
6	CH_2	100.76±11.64	1168.60±156.12	14.95±2.00	0.119
	C	94.57±12.88	1541.40±221.88	19.72±2.84	0.400
	Al	102.55±27.41	1783.50±523.46	22.82±6.70	0.065

fragment for the same targets. The temperature increases with the increase of target size for an emission of projectile fragments with charge $Z=6$ and 18, but for an emission of projectile fragment with charge Z=24 and 25, this dependence is not obvious.

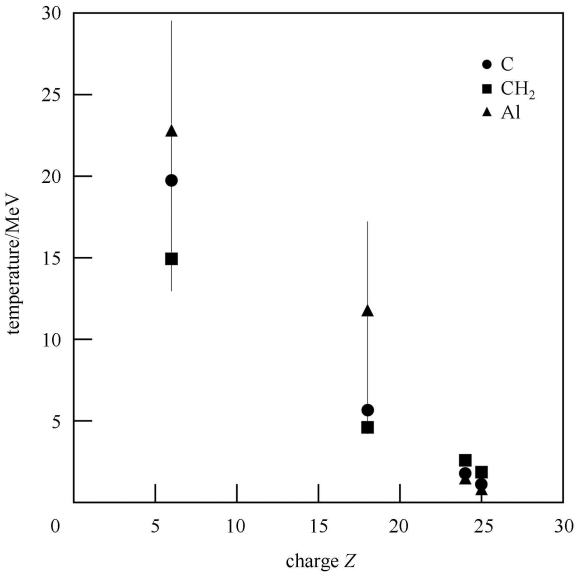

Fig. 11. The temperature derived from the distribution of p_t^2.

The temperature of the projectile fragment emission source have been investigated by different collaborations [30, 31, 39–44]. The ALADIN collaboration studied the slope temperature (T_{slope}) for the spectator decay as a function of the projectile fragment mass (A_{frag}) for spectator decays following ^{197}Au on ^{197}Au collisions; they found that there is a rapid increase of T_{slope} with projectile fragment mass, which saturates for $A_{\mathrm{frag}} \geqslant 3$ around $T_{\mathrm{slope}} \sim 17$ MeV [39, 45]. The EOS collaboration also studied the variation of the remnant temperature with the charged particle multiplicity; they found that the remnant temperature increases with increase of the charged particle multiplicity and the maximum is about 15.6±0.47 MeV [46]. These maximum temperatures are the same as our results, within experimental errors for an emission of a fragment with charge Z=6.

According to the participant-spectator concept, it is assumed that when the interaction of projectile and target nuclei takes place, the projectile and target sweep out cylindrical cuts through each other. During the separation of the spectators from the participants, there is some intercommunication, which results in the excitation of the spectators. This excitation strongly depends on the contacted area of the colliding system. The heavier fragment corresponds to the large impact parameter and small contacted areas, the lighter fragment corresponds to the smaller impact parameter and large contacted areas. So the excitation energy of the heavier fragment is less than that of the lighter fragment, which results in the temperature of an emission source of a heavier fragment being less than that of the lighter fragment.

4 Conclusions

The emission angular distribution and the transverse momentum distribution of projectile fragments produced in fragmentation of ^{56}Fe on C, Al and CH_2 targets are studied in this investigation. It is found that for the same target, the average value and width of the angular distribution decrease with the increase of the projectile fragment charge; further, for the same projectile fragment, the average value of the distribution increases and the width of the distribution decreases with increasing the target charge number. The transverse momentum distribution of the projectile fragment can be explained by a single Gaussian distribution and the averaged transverse momentum per nucleon decreases with the increase of the charge of fragment; no obvious dependence of transverse momentum on the target size is observed. The cumulated squared transverse momentum distribution of a fragment can be well explained by a single Rayleigh distribution. The temperature parameter of the emission source of projectile fragments decreases with the increase of the size of the projectile fragments.

References

1 Badhwar G D, O'Neill P M. Nucl. Tracks Radiat. Meas., 1992, **20**: 403–412
2 Giacomelli M, Skvarc J, Ilic R, Yasuda N, Sihver L. Radiat. Meas., 2003, **36**: 329–334
3 Momota S, Notani M, Ito S et al. Nucl. Phys. A, 2002, **701**: 150–155
4 Giacomelli M, Sihver L, Skvarc J, Yasuda N, Ilic R. Phys. Rev. C, 2004, **69**: 064601
5 Trautmann W. Nucl. Phys. A, 2001, **685**: 233–245
6 Wilson J W, CHUN S Y, Badavi F, Townsend L, Lamkin S L. NASA Technical Paper 3146. NASA, Langley Research Center, Hampton, Virginia. 1991
7 Sihver L, Schardt D, Kanai T. Jpn. J. Med. Phys., 1998, **18**: 1–21
8 Fasso A, Ferrari A, Ranft J, Sala P R. CERN Yellow Report 2005-10, INFN/TC-05/11. 2005
9 Wilson J W, Tripathi R K, Cucinotta F A, Shinn J L, Badavi F F, CHUN S Y, Norbury J W, Zeitlin C J, Heilbronn L, Miller J. NASA Technical Paper 3533. NASA, Langley Research Center, Hampton, Virginia. 1995
10 Kraft G. Prog. Part. Nucl. Phys., 2000, **45**: 473–544
11 WANG Ning, LI Zhu-Xia, WU Xi-Zhen. Phys. Rev. C, 2002, **65**: 064608
12 WANG Ning, LI Zhu-Xia, WU Xi-Zhen et al. Phys. Rev. C, 2004, **69**: 034608
13 Guetersloh S B, Zeitlin C, Heilbronn L, Miller J, Komiyama T, Fukumura A, Iwata Y, Murakami T, Bhattacharya M. Nucl. Instrum. Methods B, 2006, **252**: 319–332
14 La Tessa C, Guetersloh S, Heilbronn L et al. Adv. Space Res., 2005, **35**: 223–229
15 LIN Z W. Phys. Rev. C, 2007, **75**: 034609
16 Zeitlin C, Miller J, Heilbronn L, Frankel K, Gong W, Schimmerling W. Radiat. Res., 1996, **145**: 655–665
17 Zeitlin C, Heilbronn L, Miller J, Rademucher S E, Borak T, Carter T R, Frankel K A, Schimmerling W, Stronach C E. Phys. Rev. C, 1997, **56**: 388–397
18 Zeitlin C, Heilbronn L, Miller J. Radiat. Res., 1998, **149**: 560–569
19 Zeitlin C, Guetersloh S B, Heilbronn L H, Miller J. Nucl. Instrum. Methods B, 2006, **252**: 308–318
20 Webber W R, Kish J C, Schrier D A. Phys. Rev. C, 1990, **41**: 533–546
21 Napolitani P, Schmidt K H, Botvina A S, Rejmund F, Tassan-Got L, Villagrasa C. Phys. Rev. C, 2004, **70**: 054607
22 Westfall G D, Wilson L W, Lindstrom P J, Crawford H J, Greiner D E, Heckman H H. Phys. Rev. C, 1979, **19**: 1309–1323
23 Webber W R, Brautigam D A. The Astrophys. J. 1982, **260**: 894–908
24 Ferrando P, Webber W R, Goret P, Kish J C, Schrier D A, Soutoul A, Testard O. Phys. Rev. C, 1988, **37**: 1490–1501
25 Cecchini S, Chiarusi T, Giacomelli G et al. Nucl. Phys. A, 2008, **807**: 206–213
26 WANG Li-Chun, ZHANG Dong-Hai, YAN Shi-Wei et al. Acta Phys. Polon. B, 2012, **43**: 1769–1782
27 Ota S, Kodaira S, Yasuda N et al. Radiat. Meas., 2008, **43**: S195–S198
28 Greiner D E, Lindstrom P J, Heckman H H, Cork B, Bieser F S. Phys. Rev. Lett., 1975, **35**: 152–155
29 Viyogi Y P, Symons T J M, Doll P et al. Phys. Rev. Lett., 1979, **42**: 33–36
30 Brady F P, Christie W B, Romero J L et al. Phys. Rev. Lett., 1988, **60**: 1699–1702
31 Dreute J, Heinrich W, Rusch G, Wiegei B. Phys. Rev. C, 1991, **44**: 1057–1064
32 Brady F P, Christie W P, Romero J L et al. Phys. Rev. C, 1994, **50**, R525–R529
33 Rusch G, Heinrich W, Wiegel B et al. Phys. Rev. C, 1994, **49**: 901–911
34 Huntrup G, Streibel T, Heinrich W. Phys. Rev. C, 2001, **65**: 014605
35 Goldhaber A. Phys. Lett. B, 1974, **53**: 306–308
36 MA Y G et al. Phys. Rev. C, 2002, **65**: 051602
37 Bowman J D, Swiatecki W J, Tsang C F. Lawrence Berkeley Laboratory Report, 1973, LBL-2908
38 Westfall G D, Gosset J, Johansen P J, Poskanzer A M, Meyer W G, Gutbrod H H, Sandoval A, Stock R. Phys. Rev. Lett., 1976, **37**: 1202–1205
39 Odeh T et al. Phys. Rev. Lett., 2000, **84**: 4557–4560
40 Serfling V et al. Phys. Rev. Lett., 1998, **80**: 3928–3931
41 Pochodzalla J et al. Phys. Rev. Lett., 1995, **75**: 1040–1043
42 Trautmann W et al. Phys. Rev. C, 2007, **76**: 064606
43 Fritz S et al. Phys. Lett. B, 1999, **461**: 315–321
44 WANG J et al. Phys. Rev. C, 2005, **72**: 024603
45 Gaitanos T, Wolter H H, Fuchs C. Phys. Lett. B, 2000, **478**: 79–85
46 Hauger J A et al. Phys. Rev. C, 1998, **57**: 764–783